Numerical assessment of a two-phase Tesla turbine

Niknam, Pouriya H.; Talluri, Lorenzo; Ciappi, Lorenzo; Fiaschi, Daniele

DOI:
10.1016/j.applthermaleng.2021.117364

Document Version
Peer reviewed version

Citation for published version (Harvard):
Niknam, PH, Talluri, L, Ciappi, L & Fiaschi, D 2021, 'Numerical assessment of a two-phase Tesla turbine: parametric analysis', *Applied Thermal Engineering*, vol. 197, 117364.
https://doi.org/10.1016/j.applthermaleng.2021.117364

Applied Thermal Engineering

Numerical assessment of a two-phase Tesla turbine: parametric analysis

--Manuscript Draft--

Manuscript Number:	ATE-D-21-02186R1
Article Type:	Original Research Papers
Keywords:	Tesla Turbine; Two-phase; CFD; Phase interaction; Efficiency
Corresponding Author:	Daniele Fiaschi University of Florence: Universita degli Studi di Firenze Florence, ITALY
First Author:	Pouriya H Niknam, PhD
Order of Authors:	Pouriya H Niknam, PhD
	Lorenzo Talluri, PhD
	Lorenzo Ciappi, PhD
	Daniele Fiaschi, PhD
Abstract:	The scenarios on the future energy systems invariably point to heat pumps as an emerging technology to reach efficiency goals alongside energy and CO 2 reduction goals and to a progressively increasing use of chillers and refrigeration units. In this study, a technology that could enhance the efficiency of systems based on inverse cycles is studied. Particularly, the two-phase flow behaviour of a Tesla turbine is numerically investigated. The main objectives were to clarify the role of the second phase, the actual operating range, and examine the flow mixing. Two computational approaches are developed, including the CFD analysis by commercial software and a customised home built mathematical model. The calculations are performed for two-phase R404a fluid over a range of rotational speed, plate gap size, and plate roughness. All the critical liquid-vapour interactions are discussed and are determined utilising the CFD solution of the Eulerian-Eulerian approach with a frame motion technique. The other model is a homogeneous finite-difference solution, and the mass transfer is directly determined based on the phase diagram of the fluid neglecting other phase interaction parameters. Two approaches are compared to some available experimental results from the literature, revealing an excellent agreement. The results show the average power output of 0.8 Watts with a delivered torque of 3.6 mN-m at a rotational speed of about 2000 RPM. The numerical analysis explains the different effects of the two-phase conditions on the turbine efficiency, paving the way to an accurate design of boundary layer turboexpanders operating under these conditions.
Suggested Reviewers:	Vincent Lemort, PhD Professor, University of Liege: Universite de Liege vincent.lemort@uliege.be Expert in the field of ORC expanders
	Bjorn Palm, PhD Professor, KTH Royal Institute of Technology: Kungliga Tekniska Hogskolan Bjorn.Palm@energy.kth.se Expert in the field of ORC and inverse cycles
	Jacek Smolka, PhD Professor, Silesian University of Technology - Gliwice Campus: Politechnika Slaska jacek.smolka@polsl.pl Expert in the field of fluid dynamics
	Andrzej J. Nowak, PhD Professor, Silesian University of Technology - Gliwice Campus: Politechnika Slaska andrzej.j.nowak@polsl.pl Expert in the field of fluid dynamics
	Alberto Traverso, PhD Professor, University of Genoa: Universita degli Studi di Genova alberto.traverso@unige.it

	Hamidreza Mortaheb, PhD Professor, Chemistry and Chemical Engineering Research Center of Iran Mortaheb@ccerci.ac.ir Expert in modeling and multiphase flow
	Mashallah Rezakazemi, PhD Professor, Shahrood University of Technology rezakazemi@shahroodut.ac.ir expert in CFD and multiphase flow modeling
Response to Reviewers:	

Numerical assessment of a two-phase Tesla turbine: parametric analysis

Pouriya H. Niknam[1], Lorenzo Talluri[1], Lorenzo Ciappi[1], Daniele Fiaschi[1*]

[1]Dipartimento di Ingegneria Industriale, Università degli Studi di Firenze
Viale Morgagni 40, 50135 Firenze, Italy

e-mail: [1*] daniele.fiaschi@unifi.it

Abstract

The scenarios on the future energy systems invariably point to heat pumps as an emerging technology to reach efficiency goals alongside energy and CO_2 reduction goals and to a progressively increasing use of chillers and refrigeration units. In this study, a technology that could enhance the efficiency of systems based on inverse cycles is studied. Particularly, the two-phase flow behaviour of a Tesla turbine is numerically investigated. The main objectives were to clarify the role of the second phase, the actual operating range, and examine the flow mixing. Two computational approaches are developed, including the CFD analysis by commercial software and a customised home built mathematical model. The calculations are performed for two-phase R404a fluid over a range of rotational speed, plate gap size, and plate roughness. All the critical liquid-vapour interactions are discussed and are determined utilising the CFD solution of the Eulerian-Eulerian approach with a frame motion technique. The other model is a homogeneous finite-difference solution, and the mass transfer is directly determined based on the phase diagram of the fluid neglecting other phase interaction parameters. Two approaches are compared to some available experimental results from the literature, revealing an excellent agreement. The results show the average power output of 0.8 Watts with a delivered torque of 3.6 mN-m at a rotational speed of about 2000 RPM. The numerical analysis explains the different effects of the two-phase conditions on the turbine efficiency, paving the way to an accurate design of boundary layer turboexpanders operating under these conditions.

Keywords: Tesla Turbine, Two-phase, CFD, Phase interaction, Efficiency

1. Introduction

The increase of the heat pump market is testified by the sharp growth rate, which achieves more the 10% growth in the last four years. Therefore, it is expected that by 2024 the European heat pump market will double. At present, heat pumps cover only less than 10% of the heat requirements of all buildings; however, to achieve a 2050 green neutral scenario, this share is bound to drastically increase [1].

The most significant part of the heat pump market comprises the air to the air heat pump for the smallest size segment (4 – 12 kW). However, future scenarios point out a higher diffusion of bigger heat pumps to reach efficiency and energy consumption / CO_2 reduction goals. Indeed, heat pumps to have a significant impact must be applied to multifamily residential buildings and commercial buildings. Therefore, a high-potential market in the commercial size of heat pumps with capacities in the range of 20-80 kW will open. Here it is possible to find customers who are willing to spend some extra for a top-of-the-line product due to customer-appealing policies towards greener household or commercial equipment that guarantee the lowest energy consumption in the years.

Moreover, cooling is the fastest-growing use of energy in buildings: indeed, the energy demand for space cooling has more than tripled since 1990. Cooling drives the peak electricity demand, especially in hot countries, so more efficient ACs can reduce the need for new power plants to meet peak power demand [2].

A way to improve the efficiency of such systems based on inverse cycles is to utilise a two-phase expander as a replacement for the throttling valve. This kind of solution attracted extensive attention for more than one decade and even more in the last 4–5 years. Indeed, in heat pumps and refrigeration systems, the use of an expander may allow the reduction of the throttling losses by amounts that, theoretically, can reach values even slightly above 20% of the compressor power with synthetic refrigerants (HCFC, HFC, HFO) and over 30% with CO_2. [2].

Two prominent expander families can be used within an inverse cycle: the velocity types, as turbines, and the volumetric type, as scrolls, screws, vanes, and pistons. Generally, velocity types expanders are not suited for two-phase flows, as they suffer from several dynamic issues (such as very big change of volumetric flow); therefore, volumetric expanders are preferred [3].

However, in the last years, there has been an increasing interest in utilising Tesla turbines in renewable energy applications, including the small-scale power extraction units, which motivated several theoretical and experimental studies. Furthermore, amongst the other applications, this turbine has started to be also investigated for two-phase expansion processes, as testified by the recent publication on this subject [4, 5, 6].

The Tesla turbine belongs to bladeless boundary layer turbomachinery, and the working principle is based on the viscous forces on shaft-mounted parallel discs, which transfer torque, putting them in motion. Upstream the rotor, the flow is accelerated through one or more nozzles and then enters the rotor with a tangential-dominant direction. The swirling flow passes the gap between discs and moves towards the rotor outlet located around the shaft. The history of the Tesla turbine dates back to 1913, when Nikola Tesla revealed and patented the first design of this machine. [7]

Later in the years, several pieces of research were performed on the Tesla turbine, which can be classified into three major categories. The first group includes the experimental studies attempting to improve the performance of the turbine by enhancing its geometry. Some studies focused on the nozzle improvement, as testified to be the component that introduces the highest inefficiency, such as those developed by Guha et al., 2009 [8] and Neckel and Godinho, 2014 [9]. Also, several studies provided assessments of performance and efficiency under various operating conditions. Specifically, in the study of Rice et al., 1965, a wide range of feed conditions was applied to the experimental setup to evaluate the performance of the multiple-disc turbine [10]. Some other experimental studies focused on investigating the flow behaviour within the discs [11] or the proof of concept when working with organic fluids [12].

The second group comprises the theoretical studies in which the authors focused on the working principle, trying to derive reliable mathematical models. Recent research studies of this type of investigation were conducted by Sengupta and Guha, who developed mathematical models by simplified Navier–Stokes equations. They assumed a steady, incompressible and laminar flow, introducing the viscosity of the fluid and a velocity gradient near the walls. [13,14,15] On the other hand, Carey, 2010 [16] developed a model closely related to the one developed by Rice [intro 01], using body forces to represent the wall shear effects. These models considered air or water as the working fluid, while new models have been developed in recent years for the Tesla turbine utilising Organic working fluids [17, 18, 19, 20].

The third one consists of the computational fluid dynamics simulations and numerical analysis, which mainly took place within the last decade. Various fluids, mechanical design, and optimisation were evaluated through this approach. Research on a single-phase turbine operating with R404a, R134a, and R245fa as working fluids were performed using CFD studies [21]. Afterwards, the partial admission effects on the tesla turbine flow field were investigated [21, 22]. Another investigation was performed by Qi et al., who studied the disc thickness and disc spacing effect by CFD models [23] and trying to assess the optimal value for the turbine performance [24].

Most of the CFD and analytical studies were subjected to single-phase condition. A two-phase feed for the tesla turbine raises several challenges, including the phase interaction, non-homogeneous distribution of the second phase within the rotor, and fluid properties of each phase. Even the critical parameters are different from the single-phase, including the speed of sound [25]. Recently, some studies pointed out some facts about the Tesla turbine operation under two-phase conditions aiming at demonstrating the related modelling challenges. Ntatsis et al. studied different disc tip clearance referred to the steam as working fluid. The numerical simulation was performed with ANSYS Fluent, and the authors acknowledged that it is possible having two-phase. Nevertheless, they neglected this aspect and carried out the simulation in a single phase as a preliminary study [26]. Engelbrecht et al. investigated the phase change itself based on a CFD simulation using a homogeneous relaxation mode of ANSYS CFX, in which a high number of computational nodes is exploited [27]. A preliminary investigation on the effect of the gap on the turbine output torque was also performed by Papagianni et al.[28].

The literature review showed that several research studies were realised on the Tesla turbine working with single-phase conditions, and only a few preliminary studies are available for the Tesla turbine under two-phase conditions. A comprehensive assessment of the Tesla turbine in two-phase condition, including compressibility and phase-interaction sub-models, is still missing in the literature. Therefore, the main goals of this study are (i) to determine the impact of the second phase on the Tesla turbine performance through 3D-CFD simulations; (ii) to perform a parametric analysis of both the geometry and critical operational conditions to determine the optimal design for the two-phase state and (iii) to develop an innovative analytical model for two-phase Tesla turbines.

2. Methodology, CFD Model

2.0. Computational domain and settings

The computational fluid dynamics analyses were focused on the rotor of the Tesla turbine. The investigation aims at optimising the geometric parameters and the operating conditions for the maximisation of energy extraction. The geometry of the rotor (a), the trajectory of the streamlines (b), and the expansion in the Thermodynamic diagram (c) are displayed in Fig 1.

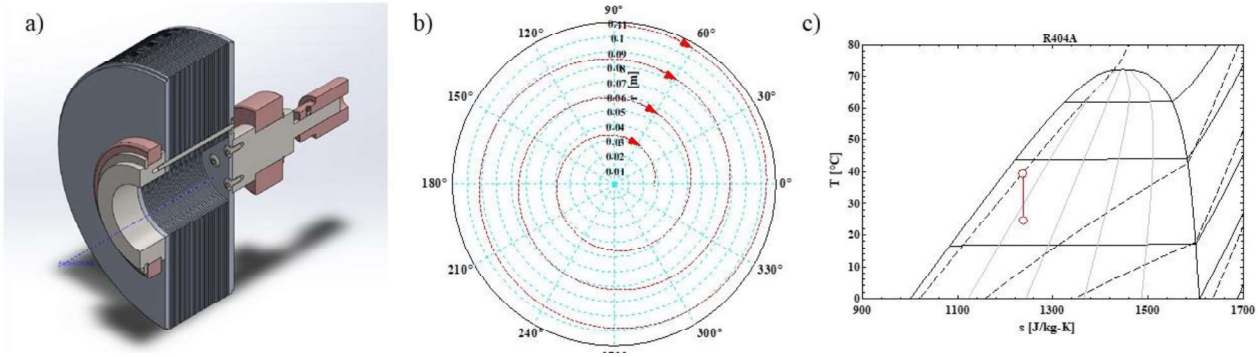

Fig. 1-(a) Schematic of Tesla turbine rotor, (b) trajectory of streamlines, and (c) expansion transformations within the rotor presented in T-s diagram

The spatial discretisation of the turbine rotor was performed with the commercial pre-processing software ANSYS ICEM 19.1, and a fully automated procedure was implemented for the creation of the computational domain and mesh.

Based on the periodically repeating pattern of the flow within the computational domain [22], the latter was limited to 1/8 of a single rotor disc passage by imposing circumferential periodicity conditions to reduce the computational requirements. In Fig. 2, the entire computational domain and its complete discretisation are illustrated. Moreover, two close-ups highlight the reduction of size achieved by applying the circumferential periodicity conditions and the element distribution in three dimensions of the disc sections.

The implemented spatial discretisation method is a finite volume with the cell-centred approach. A multi-block fully mapped mesh was created to define the computational domain for the solution of the governing equations. A mesh sensitivity analysis of the element number and distribution was performed based on previous simulations to attain the optimum configuration compromise between accuracy and computational requirements [20]. The selected mesh is comprised of about 1.135 million elements and 1.190 million nodes.

In particular, 205 nodes were set along the radial direction, 215 nodes in the circumferential direction, and 27 along the axial direction, parallel to the machine rotational axis. As concerns the main quality parameters of the mesh, the equiangular skewness is lower than 0.009207 in the entire domain, the orthogonal quality is between 0.99 and 1, and the maximum element distortion is below 3.50%.

The values of the cell dimensions at the wall boundaries were defined, limiting the maximum y^+ below the unit to achieve the proper boundary layer resolution, according to the requirements of the turbulence model. The growth ratio was set to 1.05 for the distribution of the cells along the direction of the rotational axis. This thickening of the grid perpendicular to the flow direction is pivotal in computing the variable gradients and accurately capturing the velocity profiles. In the radial and circumferential directions, from the inlet to the outlet boundaries and between the two periodic boundaries, a bi-geometric mesh law with the growth ratio of 1.1 was applied. The fine mesh adjacent to the disc walls is shown in Fig. 3, which are critical for near-wall calculations.

The CFD analyses were performed on a set of geometries characterised by fixed values of rotor inner and outer diameters equal to 20 mm and 108 mm, respectively, and different values of the gap between discs were considered, as listed in Table 1.

The discretisation of the governing equations was obtained with a cell-centred approach with the PRESTO scheme for the pressure, a third-order finite volume scheme MUSCL for the density, momentum, energy, and a second-order upwind method for the turbulent kinetic energy, specific dissipation rate, and momentum thickness. The coupled scheme was applied to correlate the corrections of velocity and pressure. The gradients of the quantities were calculated with the least-squares and cell-based method. A multiple reference frame approach with a moving reference frame was utilised to simulate the motion of the rotor, and a constant angular velocity was assigned. Finally, the governing equations were implicitly solved with the SIMPLE approach.

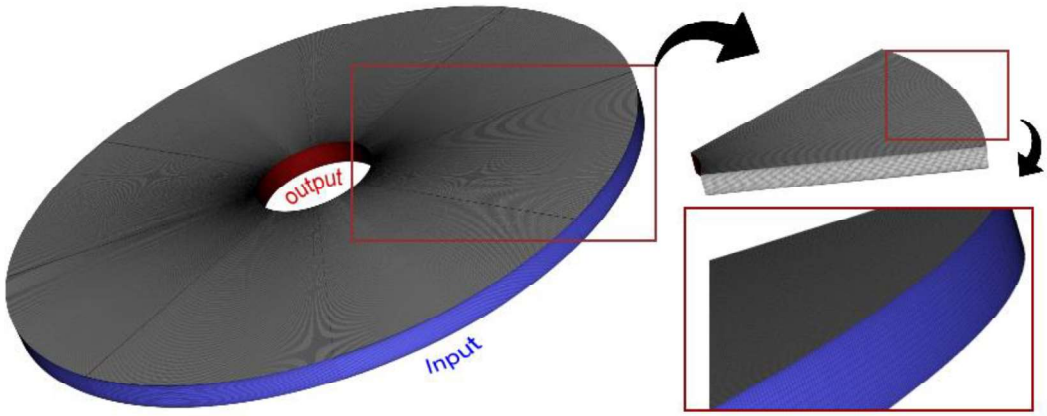

Fig. 2-Computational domain and mesh of the Tesla turbine rotor

Table 1- Dimension and boundary conditions

Item		Description
Boundary conditions	Inlet	Pressure inlet with specified radial and tangential components of flow direction with auto-adapted saturation temperature $\widehat{u_t} = +\cos(\theta)$ & $\widehat{u_r} = -\sin(\theta), \theta = [85° \dots 90°]$ If θ=85° : $\widehat{u_r}$ =0.08715574274 ; $\widehat{u_t}$ =0.99619469809
	Outlet	Pressure outlet with a fixed temperature of backflow
	wall	No-slip, with specified equivalent sand-grain roughness value and the specified rotational speed (RPM)
	Side	Rotational periodicity for the repeating unit with the angle of 45°
Dimensi	Rotor Inner diameter	20 (mm)
	Rotor outer diameter	108 (mm)
	Gap between discs	0.4, 0.6, 0.8, 1, 1.25 (mm)

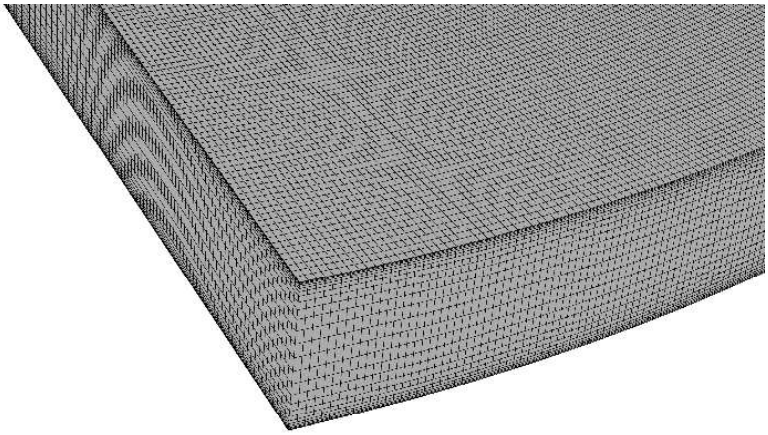

Fig. 3-Mesh close-up showing the node distribution in the three coordinate directions

2.1. Fluid Property dataset

In the present case, the phase change is expected within the computational domain having a bidirectional causality relationship with the thermodynamic condition. The real gas Peng-Robinson Equation of State (PR EoS) is used to model the density changes and considering the compressibility effects. The property data were derived using the NIST REFPROP V10.0 database in a wide range of temperature and pressures for the R404a to improve the accuracy [29]. The heat capacity (Cp), standard state enthalpy (H_0), and molecular weight (MW) are shown in Table 2.

Table 2- Thermodynamic properties-part 1 (fluid:R404a)

Properties		Gas	Liquid
Cp (kJ/kg-K)	T=309.6K	1406	1664
	T=322.4K	1815	1913
	T=338.7K	4586	3647
$H_0(J/kmol)$		3.675e+07	2.306e+07
MW $(kg/kmol)$		97.6	
Reference temperature (K)		298.15	

The parameters with a higher degree of non-linearity were fitted by the EES software [30] in the form of a polynomial, shown in Table 3. The polynomial for T^{sat} (K) is a function of the pressure (Pa), while liquid density (ρ_l), gas density (μ_g), liquid thermal conductivity (k_l), gas thermal conductivity (k_g), liquid viscosity (μ_l), and gas viscosity (μ_g) are temperature-dependent. Utilising a polynomial correlation for saturation level has been effectively applied in multiphase simulations [31, 32]. The bounds of the reference data adopted for correlations are wide enough with the approximate margin of 10 K or 5 bar of the possible temperature or pressure correlation inputs to cover different local conditions of the presented case studies, which minimises the error caused by the extrapolation. These values were imported into the CFD simulation and imposed as initial conditions in constants, piece-wise data, or fit for both liquid and gas phases.

Table 3- Thermodynamic properties-part 2 (fluid:R404a)

Polynomial Correlation	$f(x) = a_0 + a_1x + a_2x^2 + a_3x^3 + a_4x^4$						
	T^{sat} (K)	ρ_l (kg/m^3)	ρ_g (kg/m^3)	k_l (w/mK)	k_g (w/mK)	μ_l $(kg/m.s)$	μ_g $(kg/m.s)$
a_0	2.378388e02	-3.510990e05	3.487049e05	-1.705570e01	1.540322e01	-3.126793e-02	1.540322e01
a_1	7.256767e-05	4.678551e03	-4.622589e03	2.282029e-01	-2.041962e-01	4.324619e-04	-2.041962e-01
a_2	-2.588743e-11	-2.327149e01	2.297306e01	-1.136901e-03	1.014944e-03	-2.203303e-06	1.014944e-03
a_3	5.722965e-18	5.141554e-02	-5.074150e-02	2.513378e-06	-2.241063e-06	4.942640e-09	-2.241063e-06
a_4	-5.194390e-25	4.261951e-05	4.204778e-05	-2.083683e-09	1.856207e-09	-4.136043e-12	1.856207e-09
Input range	1e6…3e6 Pa	293…350 K					

2.2. Conservation Equations

The Eulerian two-fluid framework for considering the present two-phase flow problem is adopted to investigate the fluid behaviour. The mathematical models include the Eulerian two-fluid model with several sub-models to consider the phase interaction. The steady-state momentum equation for the *vapour* phase is defined as Eq. 1.

$$\nabla.\left(\alpha_v\rho_v\vec{V}_v\vec{V}_v\right) = -\alpha_g\nabla p + \nabla.\tau_v + \alpha_v\rho_v g + \vec{F}_D + \vec{F}_L + \vec{F}_{WL} + \vec{F}_{TD} \quad (1)$$

where $\dot{m}$, τ_v, g, F_D, F_L, F_{WL} and F_{TD} are mass transfer source term, vapour phase stress-strain tensor, gravity acceleration, drag force, lift force, wall lubrication force, and the turbulence dispersion force, respectively. The same equations are considered for the liquid phase.

2.3. Phase-Interactions

2.3.1 mass transfer

The liquid-vapour volumetric mass transfer is governed by the vapour transport equation based on either the Lee model or the thermal phase-change approach.

According to Eqs. 2, 3 and 4, the mass transfer equation and the evaporation-condensation rate ($\dot{m}_{lv}$ & $\dot{m}_{vl}$) in the Lee model [33] requires tuning of the coefficients (C_{lv}, C_{vl}), according to the experimental data, to match the desired rates. In these equations, the coefficients act as a surrogate for the computational cell's characteristic thermal time scale; therefore, the values depend on both the mesh resolution and fluid properties.

$$\nabla\left(\alpha_v \rho_v \vec{V}_v\right) = \dot{m}_{lv} - \dot{m}_{gv} \tag{2}$$

$$\dot{m}_{lv} = C_{lv} * \alpha_l \rho_l \frac{T_l - T^{sat}}{T^{sat}} \quad , \quad T_l > T^{sat} \tag{3}$$

$$\dot{m}_{vl} = C_{vl} * \alpha_g \rho_g \frac{T^{sat} - T_g}{T^{sat}} \quad , \quad T_g < T^{sat} \tag{4}$$

The alternative model is the thermal phase-change method, which utilises a two-resistance heat transfer model in terms of Eq. 5 and the heat from the interface to each phase is defined as in Eqs. 6 and 7. Therefore, the final mass transfer source term by considering the assumption of $T_s = T^{sat}$ is defined according to Eq. 8.

$$Q_l + Q_g = 0 \tag{5}$$

$$Q_l = h_l A_i (T_s - T_l) - \dot{m}_{lg} H_{ls} \tag{6}$$

$$Q_v = h_g A_i (T_s - T_l) - \dot{m}_{lg} H_{gs} \tag{7}$$

$$\dot{m}_{lv} = -\frac{h_l A_i (T^{sat} - T_l) + h_g A_i (T^{sat} - T_g)}{H_{gs} - H_{gs}} \tag{8}$$

The thermal phase-change approach utilised the two-resistant heat transfer model, and there was no need to tune the coefficients. In the current study, the Lee model coefficients are estimated according to the thermal phase-change model, and the results of both models are presented. More information on the evaporation-condensation model used in Fluent can be found in the literature and the Fluent theory guide [34]. In addition to the phase-change, the positioning of the bubbles is a challenging issue because the profile of the second phase is not determined by one force only. It is controlled by a combination of three lateral forces, including the lift force, the turbulent dispersion force, and the wall lubrication force, which are separately discussed.
As a result of the simulation, the Lee model coefficients are approximately adjusted based on the two-resistance thermal phase-change model results. The vapour to liquid and liquid to vapour coefficients are around 0.01 for the present case study. Therefore, either the adjusted Lee model or the thermal phase-change give the same mass transfer rates between phases and can be exploited interchangeably. Both methods apply an average volumetric phase change of 10 to 15 kg/m^3-s along with the computational model.

2.3.2 Lift force

The lift force represents the interphase actions on the bubbles caused by the liquid shear velocity field. This force is always orthogonal to the flow direction, pointing to the wall or centre of the channel and has a substantial impact on the distribution of the vapour phase between the Tesla turbine plates. It pushes the bubbles towards the walls, which is a transverse direction to the mean flow direction of the continuous phase.

The lift force is more significant for larger bubbles and has a negligible effect on small particles. According to Eq. 9, the lift force is defined in terms of slip velocity and curl of the continuous phase velocity:

$$\vec{F}_L = -C_L \alpha_g \rho_l (\vec{V}_g - \vec{V}_l) \times (\nabla \times \vec{V}_l) \quad (9)$$

in which C_L is the lift coefficient, which is calculated by Tomiyama correlation [35].

2.3.3 Wall lubrication force

Contrary to the lift force, which pushes bubbles toward the wall, the wall lubrication force tends to limit this behaviour near the walls; thus, the bubbles are concentrated in the near-wall region not immediately adjacent to the wall. This force is defined according to Eq. 10, in which the wall lubrication coefficient C_{WL} is calculated by the Hosokawa model (Eq. 11) as a function of Eötvös number (Eo) and the phase relative Reynolds number [36]. Also, the non-dimensional Eötvös number is defined according to Eq. 12 by using the surface tensions coefficient (σ), densities, and the bubble diameter.

$$\vec{F}_{WL} = C_{WL} \alpha_g \rho_l \left|(\vec{V}_g - \vec{V}_l)\right|^2 \vec{n}_w \quad (10)$$

$$C_{WL} = \max\left(\frac{7}{Re_d^{1.9}}, 0.0217 Eo\right) \quad (11)$$

$$Eo = {g(\rho_l - \rho_g) d_g^{\,2}}/{\sigma} \quad (12)$$

2.3.4 Turbulent dispersion force

The turbulent dispersion force plays the role of turbulent diffusion in dispersed flows, resulting from the turbulent fluctuations of liquid velocity and impacting the bubbles by pushing them to flow with the continuous phase. This force is calculated by either of the Simonin or Burns models, according to Eq. 13 or 14, respectively [37, 38].

$$\vec{F}_{TD} = -C_{TD} K_{gl} \frac{D_{t,gl}}{Sc} \left(\frac{\nabla \alpha_g}{\alpha_g} - \frac{\nabla \alpha_l}{\alpha_l}\right) \quad (13)$$

$$\vec{F}_{TD} = -C_{TD} K_{gl} \frac{\mu_l^t}{\rho_l Sc} \left(\frac{\nabla \alpha_g}{\alpha_g} - \frac{\nabla \alpha_l}{\alpha_l}\right) \quad (14)$$

in which C_{TD}, K_{gl}, $D_{t,gl}$, μ_l^t and Sc are constant coefficients, momentum transfer coefficient, liquid bubble dispersion scalar, turbulent viscosity of liquid phase, and Schmidt number, respectively.

2.6.5 Drag force

The drag force is taken from the Morsi-Alexander equation, according to Eqs. 15 and 16, which is applicable in a wide range of Re.

$$f = \frac{C_D Re}{24} \quad (15)$$

$$C_D = a_1 + {a_2}/{Re} + {a_3}/{Re^2} \quad (16)$$

The constants a_1, a_2 a_3 in various Re fields are available in the literature. Re is the relative Reynolds number, which is a function of the slip velocity of phases and the diameter of the bubbles (Eq. 17).

$$Re = \frac{\rho_l \left|\vec{V}_l - \vec{V}_v\right| d_v}{\mu_l} \tag{17}$$

2.7. Roughness model

The roughness value of the aluminium plates used in the prototype of the experimental study of Talluri et al. (2018) [20] on a single-phase tesla turbine is experimentally investigated in the present study. First, the surface scan was performed by Atomic Force Microscopy (AFM) method using Rasterscope C26, DME. Then, the roughness measurement was done by post-processing the results, shown in Fig. 4 and Table 4. The roughness height of the 50*50 μm^2 plate was found about 0.2 μm.

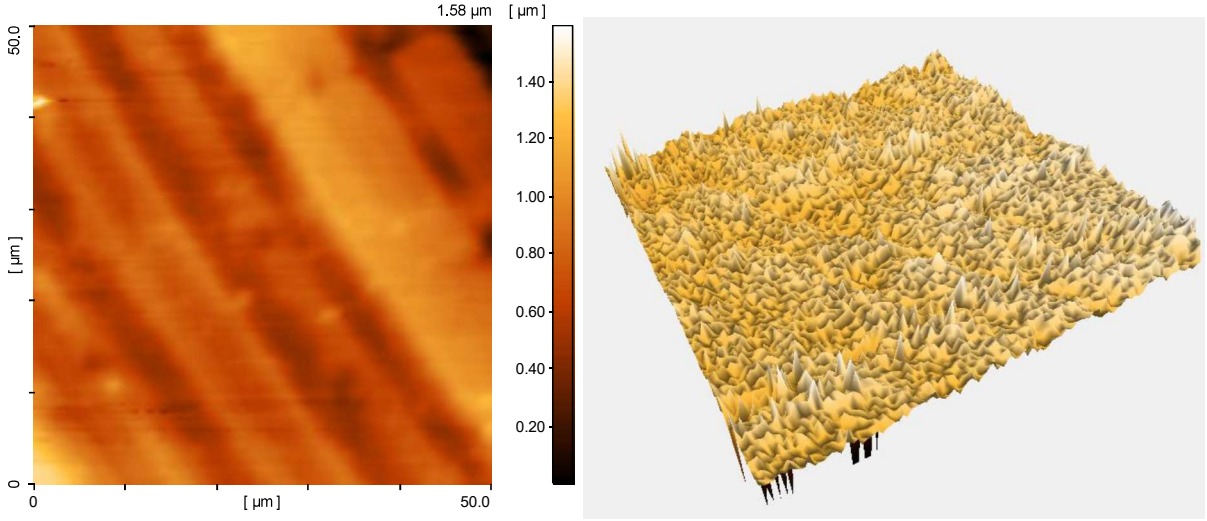

Fig. 4- Imaging analysis of the aluminium plate used for the rotor

Table 4-Properties of the realistic surface samples

property	value
Sample size [μm^2]	50×50
R_q [nm]	176
R_a [nm]	139
R_z [nm]	908
R_{sk}	0.32
R_{ku}	3.29

The roughness model for near smooth walls is based on the observation of the viscous sublayers in which the walls are virtually shifted by correcting the y^+ value in order to consider the blockage effect of the roughness and the vertical transfer of momentum according to Eq. 18:

$$y^+_{new} = y^+ + K_s^+(K_s)/2 \tag{18}$$

in which K_s^+ is the non-dimensional roughness height as a function of the equivalent sand grain roughness height (K_s), and the description can be found in the literature. K_s can be derived using the arithmetical mean deviation of roughness height R_a [39, 40, 41]:

$$K_s = \frac{2R_a}{\left(\frac{\pi}{2} - \cos^{-1}(1 - \frac{\pi^2}{16})^{1/2} - \frac{\pi}{4}(1 - \frac{\pi^2}{16})\right)} \quad (19)$$

This method is suitable for the same case study of the Tesla turbine by Rusin et al. 2019 [42]. The correlation developed by Schlichting et al. and Coleman et al. is exploited to encounter the geometric roughness height in the transition SST model [43, 44, 45]. This correlation determines the equivalent sand roughness value (K_s) using the roughness element height (k). The equivalent sand grain is calculated as 0.76 μm, which is already considered in the simulation. This vertical transfer partially alters the diffusion term in the transport equation in terms of the molecular and turbulent eddy viscosities. The ratio of equivalent roughness to the gap of the discs and the corresponding y^+ displacements in the CFD approach are shown in Fig. 5.

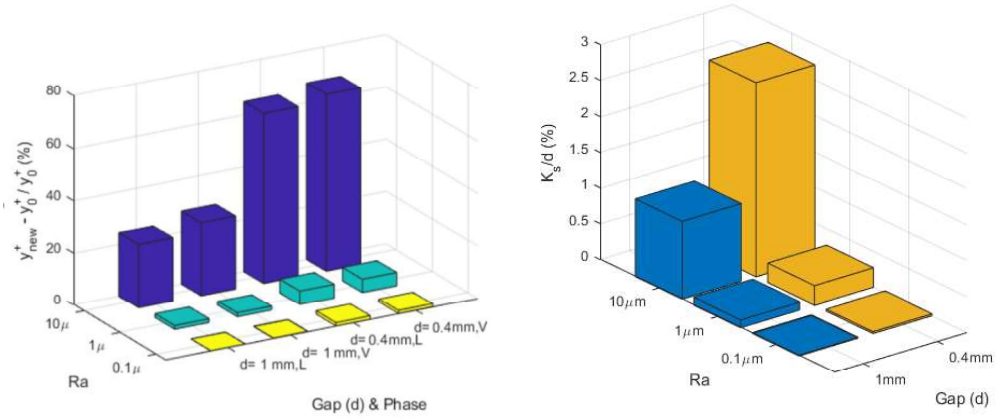

Fig. 5- Relative y^+ displacement in various case studies (left) and Relative equivalent roughness (right)

The figure shows either the increase of the roughness height or how the decrease of the distance between rotor plates increases the relative displacement compared to the y^+ with the zero-roughness assumption (y_0^+). The rationale behind this is that both high roughness (Ra) and low gap (d) contribute to a high ratio of the equivalent roughness (K_s) to the gap between discs (d).

2.8. Bubble shape and size

The bubble departure diameter of the dispersed phase plays a fundamental role in the two-phase flow and heat transfer process and has a close relationship with the interfacial area. The volume-based mass transfer and the heat transfer source terms are functions of the bubble interface area. Moreover, the area is used in other phase interaction effects, including the drag calculations. Therefore, a reliable value is required considering the bubble diameter responsible for the interfacial area. There are several approaches to assess the bubble diameter. It can be assumed either as a constant mean value or in the form of a distribution function. Also, a polydisperse model can be utilised, which applies local distribution functions known as the method of classes (CM) or the method of moments (MOM) [46, 47]. The Sauter mean diameter (SMD) using the Rosin-Rammler [48] distribution function within the range of 20-50μm is adopted in the present case study.

According to the literature, in large bubbles, with the most prominent dimension greater than 1 mm, ellipsoidal and spherical-cap shapes should be considered [34, 49], but the spherical shape is recommended in cases with relatively small-scale bubbles, including the present one.

2.9. Solver Settings

The problem is set in the steady-state pressure-based segregated 3D-solver of ANSYS Fluent V2020 R2 [34], which benefits from the Green-Gauss finite volume method. The SIMPLE algorithm is exploited for the pressure-velocity coupling and solving the Reynolds-Averaged Navier-Stokes equations. The third-order MUSCL scheme was adopted for the spatial discretisation of momentum and energy equations, while the second-order Upwind scheme and PRESTO were used for the density and the pressure, respectively. The results here presented correspond to a grid-independent solution with about 500,000 computational nodes representing the rotor geometry. The sensitivity of the solution to the mesh number is also investigated by utilising various mesh configurations. The mesh with 400,000 computational nodes has less than 0.01% of relative error for the mass balance than a more refined mesh with 1,300,000 computational nodes; therefore, the grid independence check was satisfied. The Shear Stress Transport k-ω (SST k-ω) turbulence model is applied to close the problem of the flow turbulence. According to the literature, y^+ values between 0.001 and 1 are recommended while using the transient SST turbulent model to simulate the transition location. The average value of y^+ for the selected mesh scheme prior to the displacement by the equivalent roughness model is about 0.9. The convergence criteria of 10^{-6} is maintained for the transport parameters in all case studies. Further, the contribution of the viscous heating in the energy equation, which slightly alters the temperature and the related properties caused by internal friction [50] are fully determined in the model. The utmost importance of viscous heating is also reported by Yan et al. in two-phase rotating applications, which improves the CFD result against the experimental data [51].

3. Methodology, homogeneous model

The two-dimensional numerical model for assessing the fluid dynamics of the two-phase Tesla turbine was developed in the EES environment [30]. It combines the single-phase model of the Tesla turbine, set in previous studies [12, 20], and the two-phase homogeneous model [52], where the same velocities of the two phases (gas and liquid) are assumed ($w_l = w_g = w$) [53, 54]

The following assumptions were considered:

a) Steady flow regime;

b) The viscous force is treated as a body force acting on the flow at each (r - θ) position;

c) Two-dimensional flow in terms of V_r and V_θ while $V_z = 0$;

d) Radial symmetric flow field, uniform at the inlet ($r = r_0$). The flow field is thus the same for any θ, therefore the derivative $\partial / \partial\theta = 0$ for all flow variables;

e) $(\partial p / \partial\theta)$ negligible compared to wall friction forces

According to the previous assumptions, the fundamental Navier-Stokes equations in cylindrical coordinates are reduced to the form of Eqs. 20 to 24:

Continuity

$$\frac{1}{r}\frac{\partial(r\rho_{TP}V_{r,TP})}{\partial r}=0 \qquad r\rho_{TP}V_{r,TP}=constant \tag{20}$$

Momentum, r-direction

$$V_{r,TP}\frac{\partial V_{r,TP}}{\partial r}-\frac{V_{\theta,TP}^2}{r}=-\frac{1}{\rho_{TP}}\left(\frac{\partial p}{\partial r}\right)_{TP}+f_{r,TP} \tag{21}$$

Momentum, θ-direction

$$V_{r,TP}\frac{\partial V_{\theta,TP}}{\partial r}+\frac{V_{r,TP}V_{\theta,TP}}{r}=f_{\theta,TP} \tag{22}$$

Momentum, z-direction

$$-\frac{1}{\rho_{TP}}\left(\frac{\partial p}{\partial z}\right)_{TP}=0 \tag{23}$$

Knowing the mass flow rate inside each channel, it follows that locally:

$$V_{r,TP}=-\frac{\dot{m_{tot}}}{2\pi rb\rho_{TP}} \tag{24}$$

Considering a fluid element between the two discs defines the flow channel, a control volume Q_e can be defined with base surface A_e and height b. The fluid wetted area is $A_w = 2A_e$. Therefore, the hydraulic diameter D_h is equal to 2×b. Consequently,

$$A_e=\frac{Qe}{b}=\frac{2Qe}{D_h} \qquad A_w=\frac{4Qe}{D_h} \tag{25}$$

The formulation of the viscous shear stress can be obtained considering the two-phase flow as a homogeneous flow.

Introducing the two-phase homogeneous model ($w_l = w_g = w$) [52, 53], the shear stress can be written as Eq. 26.

$$\tau_w=\frac{f_{TP}\rho_{TP}}{2}w^2=\frac{f_{TP}\rho_{TP}}{2}[(V_\theta-\omega r)^2+V_r^2] \tag{26}$$

where ρ_{TP} is the two-phase density of the fluid defined as Eq. 27:

$$\rho_{TP}=\left(\frac{x}{\rho_g}+\frac{1-x}{\rho_l}\right)^{-1} \tag{27}$$

The friction factor is calculated through Churchill correlation as Eq. 28.

$$f_{TP}=2\left[\left(\frac{8}{Re_{TP}}\right)^{12}+\frac{1}{(A+B)^{3/2}}\right]^{1/12} \tag{28}$$

where A & B are defined as:

$$A = \left[2.457 \ln\left(\frac{1}{\left(7/Re_{TP}\right)^{0.9} + \left(0.27\epsilon/D_h\right)}\right)\right]^{16} \qquad B = \left(\frac{37530}{Re_{TP}}\right)^{16} \tag{29}$$

and the two-phase Reynolds number (Re_{TP}) as a function of two-phase viscosity (μ_{TP})

$$Re_{TP} = \frac{\rho_{TP} w D_h}{\mu_{TP}} \tag{30}$$

$$\mu_{TP} = \frac{1}{2}\left[\mu_l \frac{2\mu_l + \mu_g - 2(\mu_l - \mu_g)x}{2\mu_l + \mu_g + (\mu_l - \mu_g)x} + \mu_g \frac{2\mu_g + \mu_l - 2(\mu_g - \mu_l)(1-x)}{2\mu_g + \mu_l + (\mu_g - \mu_l)(1-x)}\right] \tag{31}$$

The force resulting from wall friction is given by the product of the wall shear with the wetted area according to Eq. 32, and then the shear rate equation (Eq.26) is substituted to form Eq. 33.

$$\tau_w * A_w = F_{TP} \tag{32}$$

$$F_{TP} = \frac{f_{TP}\rho_{TP}}{2}[(V_\theta - \omega r)^2 + V_r^2] * \frac{4Q_e}{D_h} \tag{33}$$

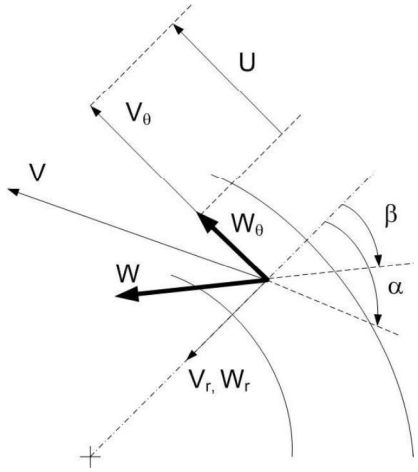

Fig. 6 – Local velocity triangle [20]

The radial and the tangential component of the force are given by:

$$\mathrm{F_r} = \mathrm{F}\cos(\beta) \qquad \mathrm{F_\theta} = -\mathrm{F}\sin(\beta) \tag{34}$$

where β is the angle between relative velocity and the radial direction. The values of $\cos\beta$ and $\sin\beta$ can thus be calculated as:

$$\cos\beta = \frac{V_r}{\sqrt{[(V_\theta - \omega r)^2 + V_r^2]}} \qquad \sin\beta = \frac{(V_\theta - \omega r)}{\sqrt{(V_\theta - \omega r)^2 + V_r^2}} \tag{35}$$

Substituting (30) in (31), a compact expression of the radial and tangential forces components are obtained:

$$F_{r,TP} = F_{TP}\cos\beta = \frac{f_{TP}\rho_{TP}}{2}[(V_\theta - \omega r)^2 + V_r^2]\frac{4Q_e}{D_h}\cos\beta = \frac{f_{TP}\rho_{TP}}{2}\frac{4Q_e}{D_h}\sqrt{[(V_\theta - \omega r)^2 + V_r^2]}V_r$$
$$F_{\theta,TP} = -F_{TP}\sin\beta = -\frac{f_{TP}\rho_{TP}}{2} * \frac{4Q_e}{D_h} * (V_\theta - \omega r) * \sqrt{(V_\theta - \omega r)^2 + V_r^2} \quad (36)$$

Dividing Eq. 33 by the mass of the fluid element between two discs, the body force term in the radial and tangential direction can be expressed as:

$$f_{r,TP} = \frac{f_{TP}}{2} * \frac{4}{D_h} * \sqrt{[(V_\theta - \omega r)^2 + V_r^2]} * V_r \quad (37)$$

$$f_{\theta,TP} = -\frac{f_{TP}}{2} * \frac{4}{D_h} * (V_\theta - \omega r) * \sqrt{(V_\theta - \omega r)^2 + V_r^2} \quad (38)$$

In order to determine the local pressure and the local derivative $(\partial \mathrm{V_r})/\partial \mathrm{r}$, Eq. 37 and Eq. 38 are substituted in Eqs. 21 and 22:

$$V_r(-\frac{V_r}{r}) - \frac{V_\theta^2}{r} = -\frac{1}{\rho_{TP}}\left(\frac{\partial p}{\partial r}\right)_{TP} + \frac{f_{TP}}{2} * \frac{4}{D_h} * \sqrt{[(V_\theta - \omega r)^2 + V_r^2]} * V_r \quad (39)$$

$$V_r\left(\frac{\partial V_\theta}{\partial r}\right)_{TP} + \frac{V_r V_\theta}{r} = -\frac{f_{TP}}{2} * \frac{4}{D_h} * (V_\theta - \omega r) * \sqrt{(V_\theta - \omega r)^2 + V_r^2} \quad (40)$$

The pressure gradients in the radial direction and the tangential velocity gradients are derived with Eqs. 41 and 42, respectively.

$$\left(\frac{\partial p}{\partial r}\right)_{TP} = \frac{\rho_{TP}V_\theta^2}{r} + \frac{\rho_{TP}V_r^2}{r} + \frac{2\rho_{TP}f_{TP}}{D_h} * \sqrt{[(V_\theta - \omega r)^2 + V_r^2]} * V_r \quad (41)$$

$$\left(\frac{\partial V_\theta}{\partial r}\right)_{TP} = -\frac{2f_{TP}}{D_h} * \frac{(V_\theta - \omega r)}{V_r} * \sqrt{(V_\theta - \omega r)^2 + V_r^2} - \frac{V_\theta}{r} \quad (42)$$

Finally, the conservation of enthalpy (H) was applied to calculate the local value of static enthalpy:

$$\mathrm{H} = \mathrm{I}_2 - \frac{\mathrm{w}^2}{2} + \frac{\mathrm{u}^2}{2} \quad (43)$$

The Euler equation defines the work output per unit mass of the expander. The efficiency calculation uses the physical properties at the inlet and the outlet of the rotor. The efficiency is defined as Eq. 45 as a function of the enthalpies, in which $H_{out,s}$ is the enthalpy at the rotor outlet for isentropic expansion. $H_{out,s}$ (P, s) is expressed as a function of entropy and pressure or can be extracted directly from the fluid P-H diagram as shown in Fig. 7.

$$\mathrm{W} = \mathrm{v_{t1}} \cdot \mathrm{u_1} - \mathrm{v_{t2}} \cdot \mathrm{u_2} \quad (44)$$

$$\eta_2 = \frac{H_{in} - H_{out}}{H_{in} - H_{out,s}} = \frac{\text{work}}{H_{in} - H_{out,s}} \quad (45)$$

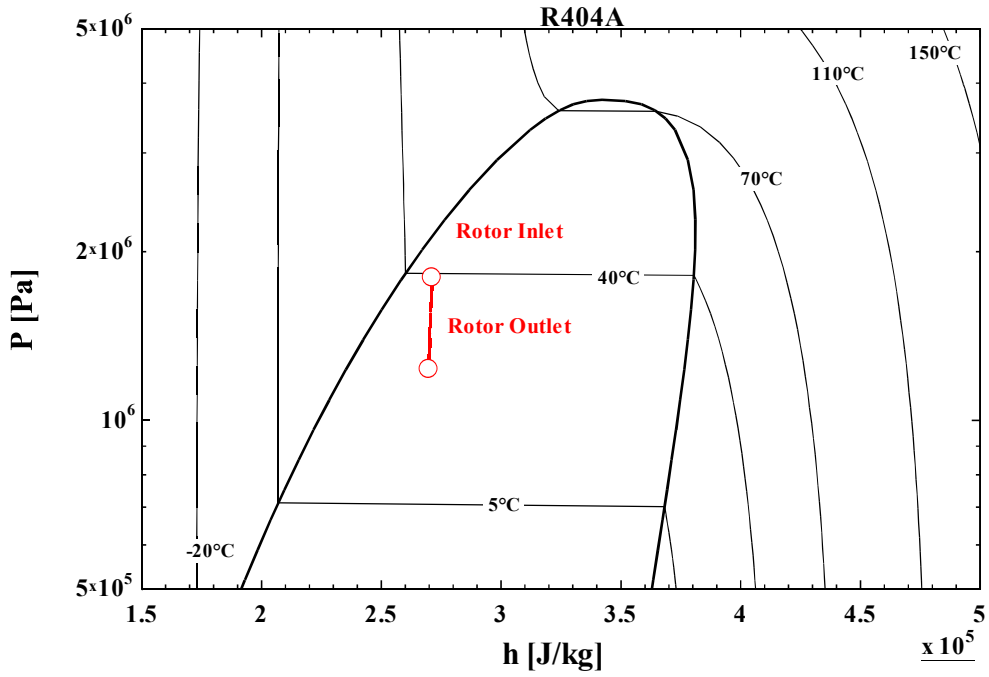

Fig. 7- Phase envelope of R404a with the analysis zone

4. Results and discussions

Both the CFD simulation and the implemented code are adopted in several case studies to investigate the behaviour of the two-phase fluid within the Tesla turbine rotor. Several cases are simulated, and the main ones are defined according to Table 5.

Table 5- CFD case studies, geometry, boundary and operating condition

Case	d [mm]	Ra [μm]	ω [rad/sec]	Mdot [kg/s]	Vin [m/s]	Vout [m/s]	Pin [Pa]	Pout [Pa]	Tin [K]	Tout [K]	Hliq_in [J/kg]	Hvap_in [J/kg]
1	0.4	0.1	220	0.0016	26.858	5.8570	2281353	2099370	322.50	318.98	280408.1	429736.6
2	0.6	0.1	220	0.0022	26.810	6.1237	2282745	2098012	322.43	318.98	280400.4	429722.7
3	1	0.1	220	0.0032	26.801	6.4062	2274164	2098889	322.53	318.98	280360.6	429707.4
4	1.25	0.1	220	0.0041	26.835	6.6197	2282274	2098313	322.40	318.98	280382.2	429707.1
5	1	0.1	140	0.0842	22.814	11.676	2281274	2101000	322.63	318.99	280765.4	430052.6
6	1	0.1	180	0.0282	23.462	9.1927	2285021	2099832	322.58	318.97	280668.0	429957.8
7	0.4	1	220	0.0016	25.713	5.7078	2281992	2099338	322.49	318.98	280402.9	429725.9
8	0.4	10	220	0.0016	25.435	4.4314	2279917	2099565	322.53	318.99	280428.0	429752.2
9	0.4	50	220	0.0016	25.513	5.5343	2280300	2099314	322.53	318.99	280399.8	429728.3

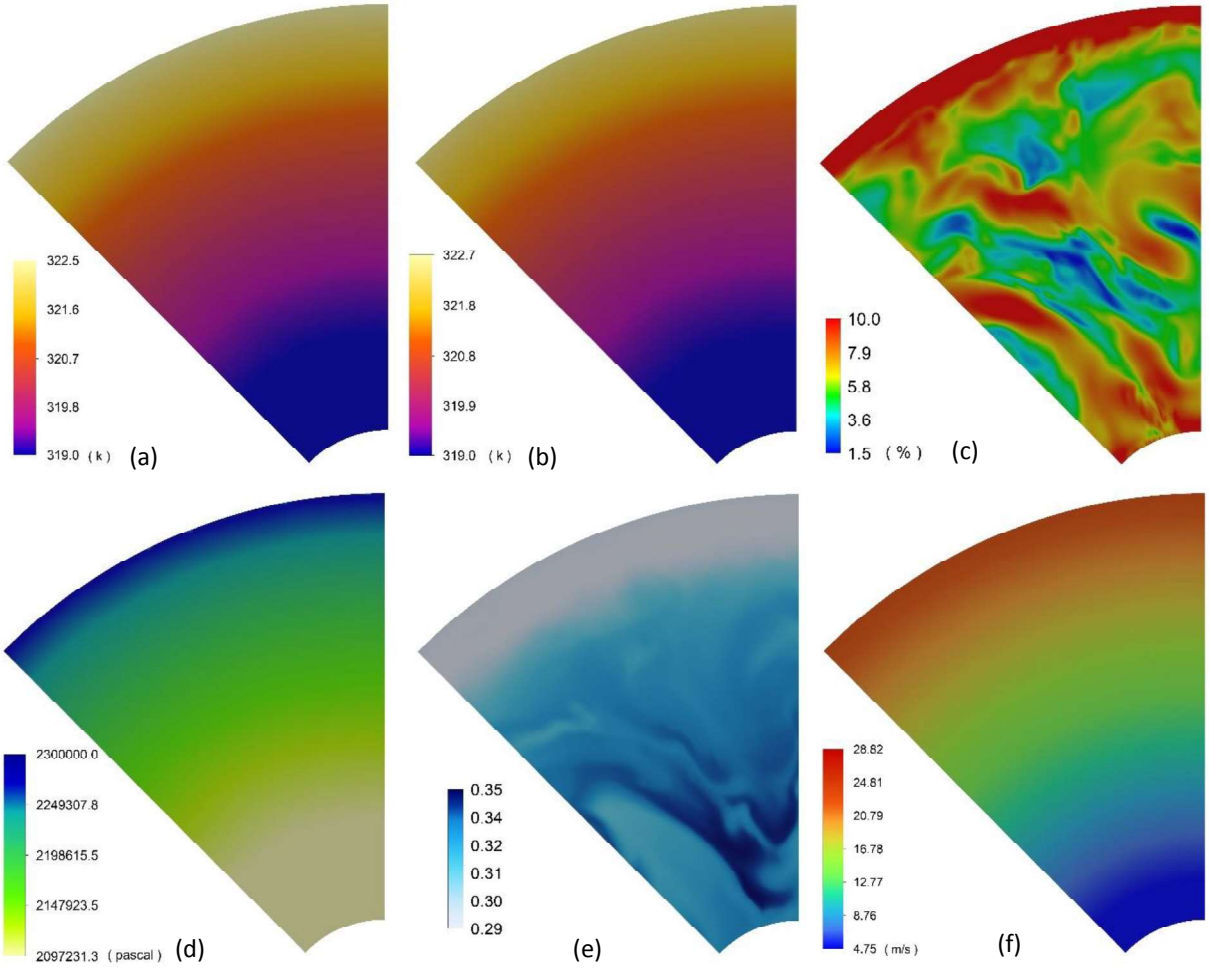

Fig. 8- Contours of the key thermodynamic parameters corresponding to the two-phase flow through the rotor: temperature (a), saturation temperature (b), turbulent intensity (c), static pressure (d), vapour fraction (e), absolute velocity (f)

The static temperature, saturation temperature, turbulence intensity, pressure, vapour-phase fraction, and velocity contours are driven from the CFD simulation shown in Fig. 8. The temperature practically corresponds to the saturation value (which is pressure-dependent) in the whole field. Thus, it demonstrates the two-phase (saturation) condition from intake to outlet of the rotor.

Although the pressure is slightly decreasing (Fig. 8d), the saturation temperature is varied accordingly. The turbulent intensity (Fig. 8c) shows the local vorticities and non-homogeneous distribution of the turbulent parameter inside the rotor, having the same pattern as the second-phase distribution (e.g., vapour) depicted in Fig. 8e, which locally alters the forces between fluid and discs. The higher viscous heating contributes to a higher formation of flow vortices, reported by Alonso et al. 2019 [54] for turbulent flows. The velocity field is shown in Fig. 8f, which continuously decreases in a notable order behaviour.

The temperature, pressure, and overall velocity of the two-phase fluid are calculated at three different rotational speeds, which radial profiles are shown in Fig. 9a, 9b, and 9c, respectively. Although the pressure-boundary conditions are fixed, the pressure and temperature behaviours are different, with a slightly larger decreasing gradient at the entrance. Furthermore, the higher rotational speed brings a higher velocity gradient along the rotor.

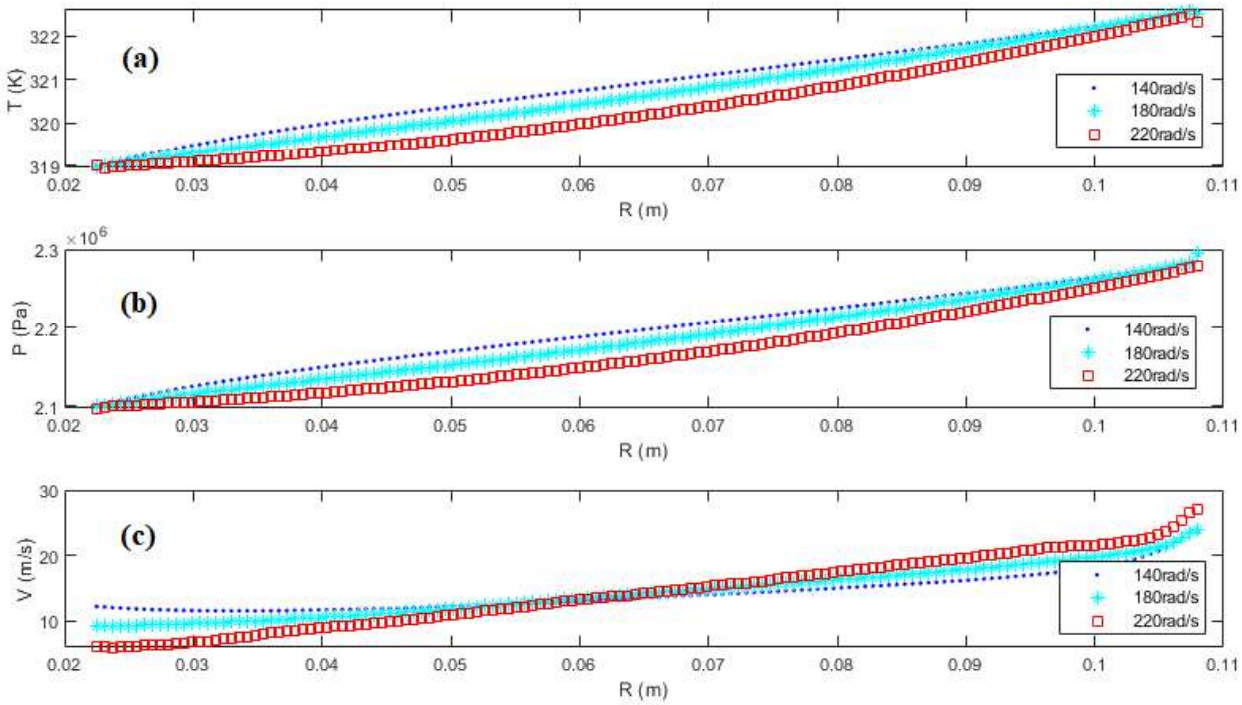

Fig. 9-Temperature (a), pressure (b) and absolute velocity (c) profile along the radius for a two-phase case study with different values of rotational speed

The crucial parameter of the turbine is the momentum and the corresponding power and efficiency, which identifies the performance of the expander. The momentum is generated by the moving two-phase fluid and puts the disc into rotation. Both approaches derive the parameters. The momentum is derived directly from the CFD solution in terms of viscous momentum and pressure momentum, without particular post-calculations. In the implemented code, the velocity is calculated, which is also used to calculate the momentum and the extracted power accordingly.

The torque value (τ) is calculated in the CFD post-processing using the overall momentum on both full-circular walls. Also, the power (W), calculated by using the predefined rotational speed (ω [rad/sec]) and the

$$W = \tau \cdot \omega \tag{40}$$

The comparison of velocity ratio and mass flow in various RPM conditions is presented in Fig. 10. The mass flow rate is the common assumption of both 1D and CFD models. In other words, the CFD-calculated mass flow rate is determined as 1D model input, and the velocity profiles are extracted from both models.

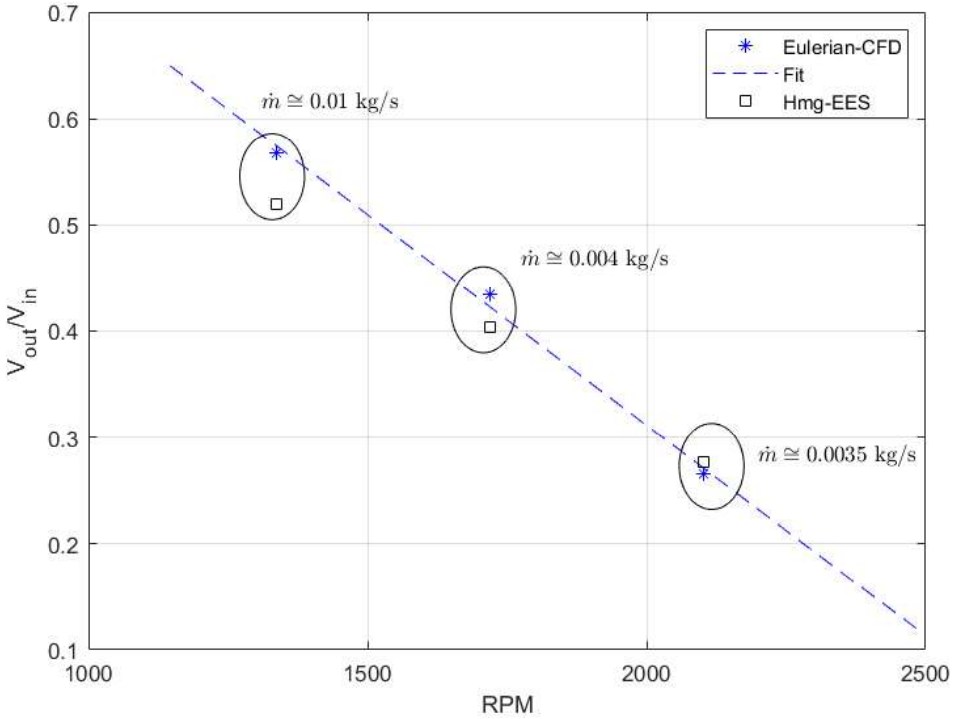

Fig. 10-Velocity ratio at various values of rotational speed

The model's sensitivity to the roughness height is reported in Fig. 11, revealing that the prediction of the homogeneous model is significantly different from the CFD results, which are more sensitive to the roughness heights. Higher roughness leads to larger friction, which contributes to larger viscous force, thus leading to higher momentum and power. The average logarithmic slope is found at about 0.036.

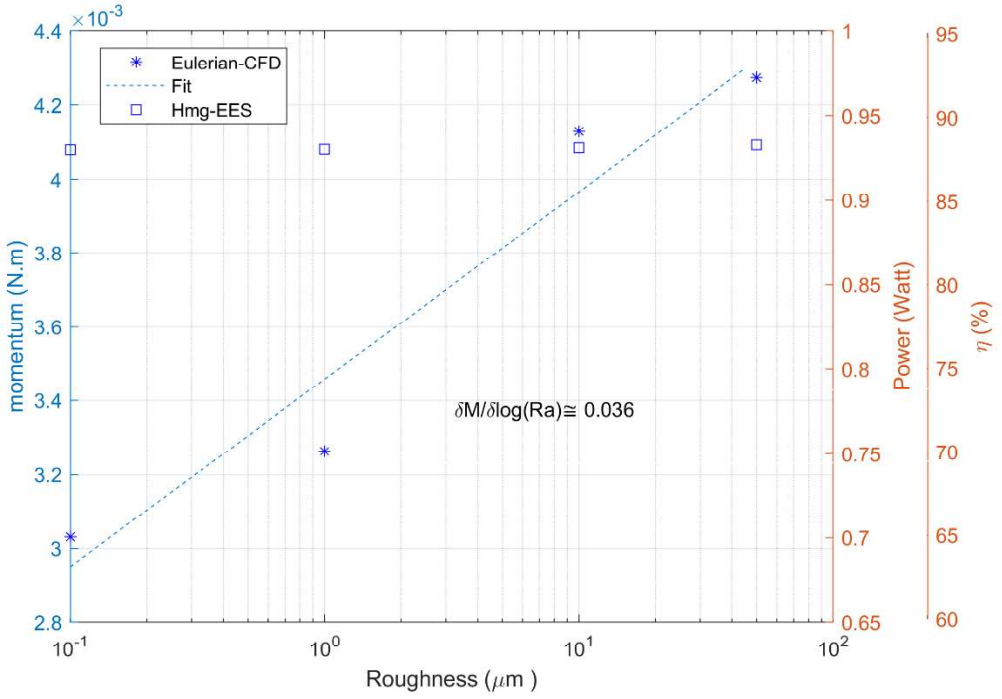

Fig. 11-Effect of boundary condition on the hydrodynamic of two-phase flow in the rotor

The 2D contour of the second phase is shown in Fig. 12, which reveals the non-uniform distribution of the second phase between the plates. Due to the wall lubrication and the turbulent dispersion forces, the bubbles

remain apart from the wall. This phase separation gradually increases as the two-phase fluid moves towards the rotor outlet.

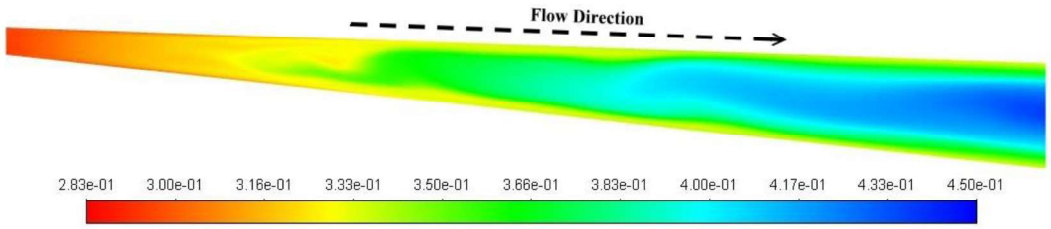

Fig. 12- Second-phase void fraction over the plane perpendicular to the discs (symmetry boundary)

Moreover, to determine how the rotor changes the vapour quality of the two-phase flow, a comparison of four case studies with different feed qualities are determined. The results are depicted in Fig. 13, in which both the output quality and the void fraction are slightly higher than the input.

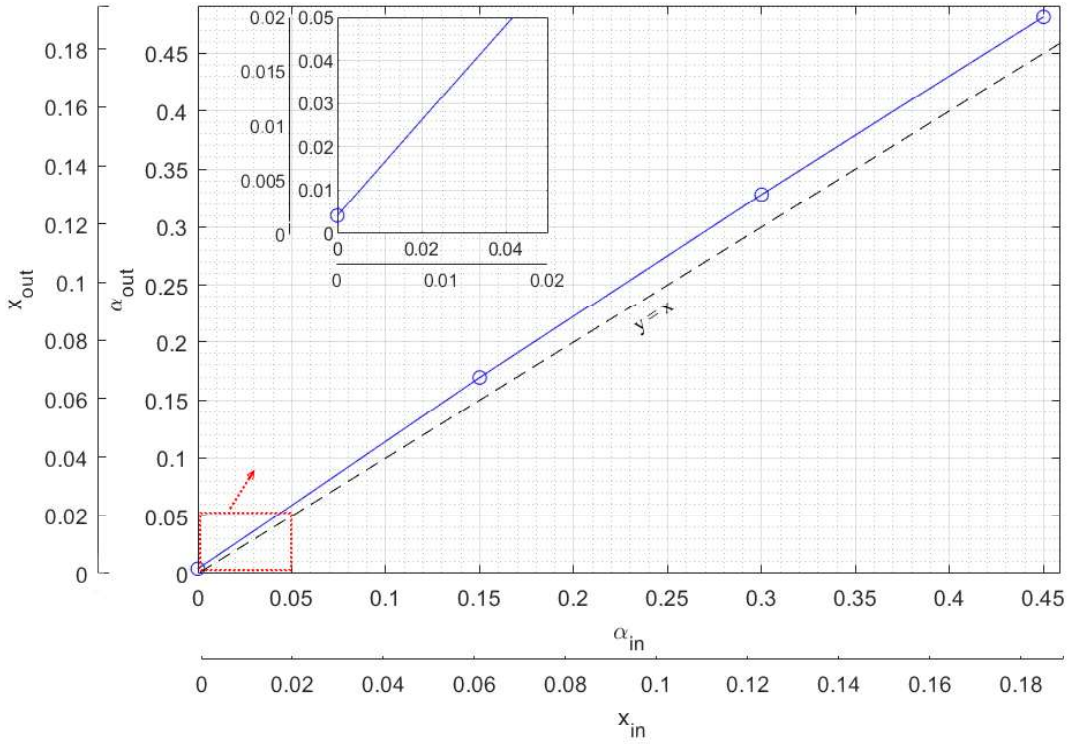

Fig. 13- Vapour quality (x) and void fraction (α) at the input and output of the rotor section of the Tesla turbine

The sensitivity of the two-phase model to the gap between the disc and the rotational speed is shown in Fig. 14. The turbine rotor tends to gain more impact in configuration with a wider space between the plates and operating at a lower rotational speed.

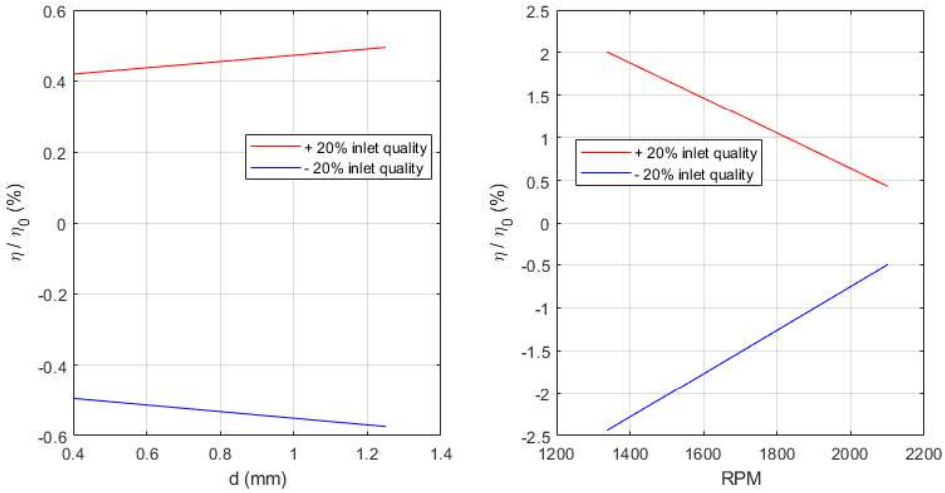

Fig. 14- sensitivity of the turbine efficiency to the inlet vapour quality (η_0 corresponds to inlet vapour quality of 0.098)

The non-homogeneous profile is discussed in both the radial and perpendicular directions. Therefore, it is essential to investigate the sensitivity of the key parameters of the two-phase flow to the gap between the plates. The comparison of mass flow at four different gap values (0.4, 0.6, 1, 1.25mm) is shown in Fig 15, while the inlet and the outlet pressure boundaries are fixed for all. Increasing the gap increases the inlet area, as well as the mass flow rate. The increase of the latter increases both the velocity ratio and the exploited momentum by the walls. Reasonable compatibility is found between the two models in terms of the velocity ratio. The discrepancy stems from different roughness models, non-homogeneous distribution of the second-phase, viscous heating, and turbulent dispersion along the rotor, all of which are neglected in the homogenous models while they are fully considered in the CFD approach. As a result, the homogenous model overestimates the rotor momentum at about 20%. The difference is negligible in lower distances between the plates.

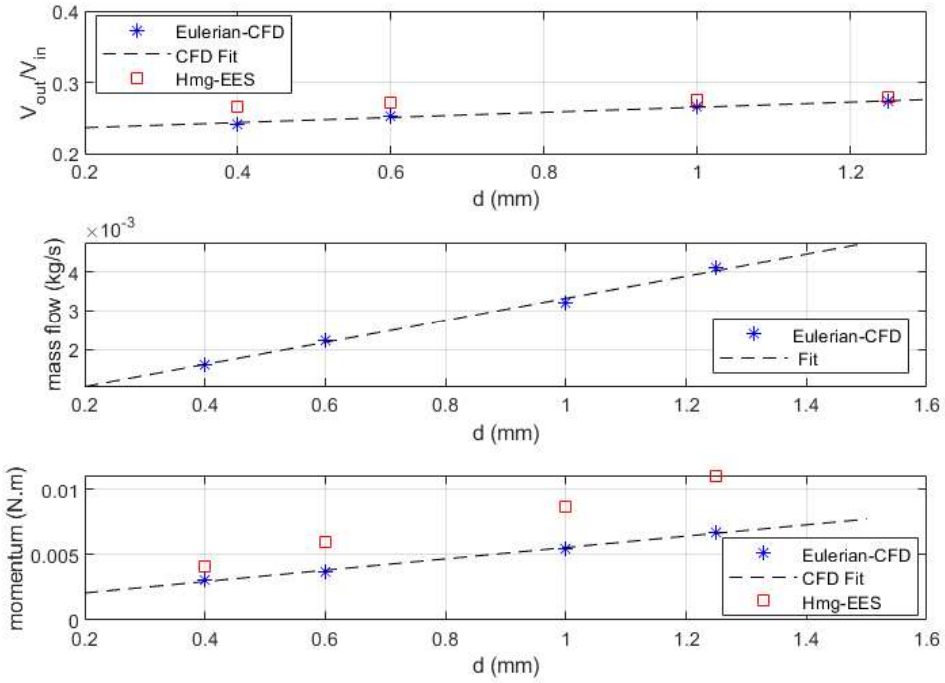

Fig. 15- The effect of the plate gap on the performance of the turbine

5. Conclusions

A numerical study is carried out using both a CFD approach and a homogeneous analytical model. The goal was comparing the performance of two models, simulate the two-phase operation of the Tesla turbine, and assess the sensitivity of the rotor to the space between the disc, roughness, and rotational speed. The comprehensive 3D CFD considers the phase interaction, with sub-models dedicated to the heat & mass transfer, roughness and turbulence, while the homogeneous model is based on the key phenomena of heat and mass transfer and friction. The results show a good agreement between the two models. Although the vapour phase along the rotor is non-homogeneous in CFD, the results are comparable, with a relative difference of 5% for the velocity and 20% for the momentum.

Moreover, the role of the roughness is discussed in detail, and it is crucial at lower gaps between the discs. Finally, the effect of the secondary phase on the performance of the Tesla turbine is investigated in various geometries at different rotor gap. The two-phase simulations revealed the average power output of 0.8 Watts with a delivered torque of 3.6 mN-m at a rotational speed of about 2000 RPM.

6. Nomenclature

Roman and Greek symbols

C_p = Heat Capacity
H = Enthalpy
H_0 = Standard state Enthalpy
hmg = Homogeneous
k = Thermal conductivity
MW = Molecular weight
MUSCL = Monotonic upstream-centred scheme
P = Pressure
R_a = Arithmetical mean deviation of the assessed profile
R_{ku} = Kurtosis
R_q = Root mean squared of the assessed profile
R_{sk} = Skewness
R_z = Maximum Height of the Profile
T = Temperature
$\vec{V}$ = Phase velocity
W = Work
x = Vapour quality
y_0^+ = Basic y^+ with zero roughness
α = Volume fraction (void fraction)
ρ = Density
τ = Torque
τ_w = Sheat stress
ω = Rotational speed

Subscripts and superscripts

D = Drag
L = Lift
l = Liquid phase
lv = Liquid to vapour
r = Radial
s = Isentropic
sat = Saturation
TD = Turbulent dispersion
Tot = Total
TP = Two-phase
v = Vapour phase
Vl = Vapour to liquid
WL = Wall turbulent
θ = Angular

7.References

[1] EHPA (European Heat Pump Association) The European heat pump market has achieved double-digit growth for the fourth year in a row, https://www.ehpa.org/market-data/ (2019). last access February 15, 2021

[2] https://www.iea.org/reports/the-future-of-cooling

[3] Galoppi G., Secchi R., Ferrari L., Ferrara G., Karellas S., Fiaschi D., Radial piston expander as a throttling valve in a heat pump: Focus on the 2-phase expansion, *International Journal of Refrigeration*, 82, 2017.

[4]] M. Imran, M. Usman, B.S. Park, D.H. Lee, Volumetric expanders for low grade heat and waste heat recovery applications, *Renew. Sustain. Energy Rev*, 57 (2016), pp. 1090-1109.

[5] A. Renuke, A. Vannoni, M. Pascenti, A. Traverso, Experimental and Numerical Investigation of Small Scale Tesla Turbines, GT2019-91352, ASME Turbo Expo 2019, Phoenix (AZ)

[6] Aghagoli A., Sorin M., CFD modelling and exergy analysis of a heat pump cycle with Tesla turbine using CO_2 as a working fluid, *Applied Thermal Engineering*, 178, 2020.

[7] Sheikhnejad Y., Simoes J., Martins N., Introducing Tesla turbine to enhance energy efficiency of regrigeration cycle, *Energy Reports*, 6, 2020.

[8] Tesla, N. Turbine. U.S. Patent 1,061,206, 6 May 1913.

[9] Guha A, Smiley B, "Experiment and analysis for an improved design of the inlet and nozzle in Tesla disc turbines", in: *Proc. IMechE, Part A: J. Power and Energy*, Vol. 224, pp. 261–277, 2009.

[10] Neckel AL, Godinho M, "Influence of geometry on the efficiency of convergent–divergent nozzles applied to Tesla turbines", in: *Experimental Thermal and Fluid Science*, Vol. 62, pp. 131–140, 2014.

[11] Rice, W. (1965). An analytical and experimental investigation of multiple-disk turbines.

[12] Schosser C., Lecheler S., Pfizner M., 2014, A test rig for the investigation of the performance and flow field of Tesla friction turbines, *Proceedings of ASME Turbo Expo 2014: Turbine Technical Conference and Exposition*, Dusseldorf.

[13] Talluri L., Dumont O., Manfrida G., Lemort V., Fiaschi D., Experimental investigation of an Organic Rankine Cycle Tesla turbine working with R1233zd(E), Applied Thermal Engineering, 174, 2020.

[14] Sengupta, S., & Guha, A. (2012). A theory of Tesla disc turbines. Proceedings of the Institution of Mechanical Engineers, Part A: Journal of Power and Energy, 226(5), 650-663.

[15] Guha, A., & Sengupta, S. (2013). The fluid dynamics of the rotating flow in a Tesla disc turbine. European Journal of Mechanics-B/Fluids, 37, 112-123.

[16] [15] Sengupta, S., & Guha, A. (2013). Analytical and computational solutions for three-dimensional flow-field and relative pathlines for the rotating flow in a Tesla disc turbine. Computers & Fluids, 88, 344-353.

[17] Carey, V. P. (2010). Assessment of Tesla turbine performance for small scale Rankine combined heat and power systems. Journal of Engineering for Gas Turbines and Power, 132(12).

[18] Song J., Gu C.W., Li X.S., 2017, Performance estimation of Tesla turbine applied in small scale Organic Rankine Cycle (ORC) system, Appl. Therm. Eng., 110: 318–326.

[19] Song J, Ren X D, Li XS., Gu CW., Zhang MM., 2018, One-dimensional model analysis and performance assessment of Tesla turbine, Applied Thermal Engineering, 134: 546-554.

[20] Talluri, L., Fiaschi, D., Neri, G., & Ciappi, L. (2018). Design and optimisation of a Tesla turbine for ORC applications. Applied energy, 226, 300-319.

[21] Manfrida G., Talluri L., 2019. Fluid dynamics assessment of the Tesla turbine rotor, *Thermal Science*, 23: 1-10.

[22] Ciappi, L., Fiaschi, D., Niknam, P. H., & Talluri, L. (2019). Computational investigation of the flow inside a Tesla turbine rotor. Energy, 173, 207-217.

[23] Pacini L., Ciappi L., Talluri L., Fiaschi D., Manfrida G., Smolka J., Computational investigation of partial admission effects on the flow field of a Tesla turbine for ORC applications, Energy, 212, 2020.

[24] Qi, W., Deng, Q., Jiang, Y., Yuan, Q., & Feng, Z. (2019). Disc Thickness and Spacing Distance Impacts on Flow Characteristics of Multichannel Tesla Turbines. Energies, 12(1), 44.

[25] Qi, W.J.; Deng, Q.H.; Feng, Z.P.; Yuan, Q. Influence of disc spacing distance on the aerodynamic performance and flow field of Tesla turbines. In Proceedings of the ASME Turbo Expo 2016, Seoul, Korea, 13–17 June 2016.

[26] Niknam, P. H., Fiaschi, D., Mortaheb, H. R., & Mokhtarani, B. (2017). An improved formulation for speed of sound in two-phase systems and development of 1D model for supersonic nozzle. Fluid Phase Equilibria, 446, 18-27.

[27] Ntatsis, K. C., Chatziangelidou, A. N., Efstathiadis, T. G., Gkoutzamanis, V. G., Silvestri, P., & Kalfas, A. I. CFD ANALYSIS OF A TESLA TURBOEXPANDER USING SINGLE PHASE STEAM.

[28] Engelbrecht, E. G., Giakoumis, Z., Sidiropoulos, S., Chasoglou, A., & Chokani, N. (2019). Modelling phase change in a novel turbo expander for application to heat pumps and refrigeration cycles. In E3S Web of Conferences (Vol. 113, p. 03012). EDP Sciences.

[29] Papagianni, A., Efstathiadis, T., Gaitanis, A., & Kalfas, A. (2019). Modelling of a Tesla turbine gap between the rotor disks. In E3S Web of Conferences (Vol. 113, p. 03013). EDP Sciences.

[30] Lemmon, E.W., Bell, I.H., Huber, M.L., McLinden, M.O. NIST Standard Reference Database 23: Reference Fluid Thermodynamic and Transport Properties-REFPROP, Version 10.0, National Institute of Standards and Technology, Standard Reference Data Program, Gaithersburg, 2018.

[31] F-Chart Software, [Online]. Available: http://www.fchart.com/ees/pro-comm-versions.php.

[32] Niknam, P. H., Mortaheb, H. R., & Mokhtarani, B. (2018). Dehydration of low-pressure gas using supersonic separation: Experimental investigation and CFD analysis. Journal of Natural Gas Science and Engineering, 52, 202-214.

[33] Niknam, P. H., Fiaschi, D., Mortaheb, H. R., & Mokhtarani, B. (2019). Numerical investigation of multiphase flow in supersonic separator considering inner body effect. Asia‐Pacific Journal of Chemical Engineering, 14(6), e2380.

[34] Wen Ho Lee. A pressure iteration scheme for two-phase flow modelling. Multiphase transport fundamentals, reactor safety, applications, 1:407–431, 1980.

[35] ANSYS Fluent Tutorial Guide. July 2020; ANSYS, Inc. Release 2020 R2

[36] Tomiyama, A., Tamai, H., Zun, I., & Hosokawa, S. (2002). Transverse migration of single bubbles in simple shear flows. Chemical Engineering Science, 57(11), 1849-1858.

[37] Hosokawa, S., Tomiyama, A., Misaki, S., & Hamada, T. (2002, January). Lateral migration of single bubbles due to the presence of wall. In ASME 2002 Joint US-European Fluids Engineering Division Conference (pp. 855-860). American Society of Mechanical Engineers Digital Collection.

[38] Simonin, O., & Viollet, P. L. (1990). Modelling of turbulent two-phase jets loaded with discrete particles. Phenomena in multiphase flows, 1990, 259-269.

[39] Burns, A. D., Frank, T., Hamill, I., & Shi, J. M. (2004, May). The Favre averaged drag model for turbulent dispersion in Eulerian multiphase flows. In 5th international conference on multiphase flow, ICMF (Vol. 4, pp. 1-17). ICMF.

[40] Borate, H. P., Misal, N. D., & Lam, P. (2012). An effect of surface finish and spacing between discs on the performance of disc turbine. Int. J. Applied Research In Mechanical Engineering (IJARME), 2(1), 25-30.

[41] Rusin, K., Wróblewski, W., & Strozik, M. (2018, October). Experimental and numerical investigations of Tesla turbine. In Journal of Physics: Conference Series (Vol. 1101, No. 1, p. 012029). IOP Publishing.

[42] Dutta, R., Nicolle, J., Giroux, A. M., & Piomelli, U. (2016, November). Evaluation of turbulence models on roughened turbine blades. In IOP Conference Series: Earth and Environmental Science (Vol. 49, No. 6, p. 062007).

[43] Rusin, K., Wróblewski, W., & Strozik, M. (2019). Comparison of methods for the determination of Tesla turbine performance. Journal of Theoretical and Applied Mechanics, 57.

[44] Coleman, H. W., Hodge, B. K., & Taylor, R. P. (1984). A re-evaluation of Schlichting's surface roughness experiment.

[45] Schlichting, H. (1936). Experimentelle untersuchungen zum rauhigkeitsproblem. Archive of Applied Mechanics, 7(1), 1-34.

[46] Adams, T., Grant, C., & Watson, H. (2012). A simple algorithm to relate measured surface roughness to equivalent sand-grain roughness. International Journal of Mechanical Engineering and Mechatronics, 1(2), 66-71.

[47] Askari, E., Proulx, P., & Passalacqua, A. (2018). Modelling of Bubbly Flow Using CFD-PBM Solver in OpenFOAM: Study of Local Population Balance Models and Extended Quadrature Method of Moments Applications. ChemEngineering, 2(1), 8.

[48] P.G. Saffman. On the rise of small air bubbles in water. Journal of Fluid Mechanics, 1:249–275, 1956.

[49] Rosin, P.A.U.L., 1933. Laws governing the fineness of powdered coal. Journal of Institute of Fuel, 7, pp.29-36.

[50] Pan, L.M., Tan, Z.W., Chen, D.Q. and Xue, L.C., 2012. Numerical investigation of vapor bubble condensation characteristics of subcooled flow boiling in vertical rectangular channel. Nuclear engineering and design, 248, pp.126-136.

[51] Sunden, B., 1992. Viscous heating in forced convective heat transfer across a circular cylinder at low Reynolds number. International journal for numerical methods in engineering, 35(4), pp.729-736.

[52] Yan, W., Xiao-Dong, R., Xue-Song, L. and Chun-Wei, G., 2018. Numerical investigation of air–oil–thermal coupling mechanism in floating ring bearings. Journal of Tribology, 140(3).

[53] Talluri L., Niknam P., Copeta A., Amato M., Iora P., Uberti S., Invernizzi C., Di Marcoberardino G., Pacini L., Manfrida G., Fiaschi D., A revised Tesla turbine concept for 2-phase applications, 100% RENEWABLE: Strategies, technologies and challenges for a fossil free future – Applied Energy Symposium (ICAE), Pisa, Italy, October 25th – 30th, 2020.

[54] Awad MM., Muzychka YS., Two-phase flow modeling in microchannels and minichannels, Heat Transfer Engineering, 31, (2010).

[55] Li X., Hibiki T., Frictional pressure drop correlation for two-phase flows in mini and micro multi channels, App. Thermal Eng., 16, (2017).

[56] Alonso, D.H., de Sá, L.F.N., Saenz, J.S.R. and Silva, E.C.N., 2019. Topology optimisation based on a two-dimensional swirl flow model of Tesla-type pump devices. Computers & Mathematics with Applications, 77(9), pp.2499-2533.